J. Fluid Mech. (1991), *vol.* 229, *pp.* 659–674
Printed in Great Britain

Bubble rise under an inclined plate

By T. MAXWORTHY
Departments of Aerospace and Mechanical Engineering, University of Southern California, Los Angeles, CA 90089-1191, USA

(Received 13 August 1990 and in revised form 3 January 1991)

We extend existing measurements of bubble rise velocity or, equivalently, drag in the spherical-cap regime to include the effects of rise under an inclined plate which both changes the bubble shape and the effective buoyancy force in the direction of bubble motion. As found previously for rise in inclined tubes for example (Zukoski 1966) there is an angle of inclination for which the rise velocity is a maximum. We propose, also, an inviscid model that appears to describe the results adequately, as is the case for the spherical-cap regime in an extended fluid (Davies & Taylor 1950).

1. Introduction

When a bubble rises in an extended fluid its characteristics are reasonably well understood and have been the subject of numerous studies (see Clift, Grace & Weber 1978 for a comprehensive review). In particular, it is known that if the Bond Number $g\Delta\rho D_e^2/\sigma$ is greater than 40 and the Reynolds number $(U_0 D_e/\nu)$ is greater than 150 the regime of 'inviscid', spherical-cap bubbles is reached and simple results are obtained that have been confirmed many times. Here g is the acceleration due to gravity; $\Delta\rho$ the density difference between the bubble and its ambient fluid; D_e is the equivalent spherical diameter, i.e. the bubble volume (V) is $\frac{1}{6}\pi D_e^3$; σ is the surface tension; U_0 the velocity of rise of the bubble and ν the kinematic viscosity of the surrounding fluid. Thus the seminal calculation of Davies & Taylor (1950) gives the velocity of rise as:

$$U_0 = \tfrac{2}{3}(gR)^{\frac{1}{2}} \tag{1}$$

for an air bubble rising in a low viscosity fluid such as water, where R is the radius of curvature of the central part of the spherical cap (see comments on this calculation in §§4 and 5). Improvements (Collins 1966) on this result are also within the experimental scatter and appear to describe the experimental results slightly better, although Clift *et al.* (1978) suggest that the simpler Davies–Taylor result is more than adequate for most purposes. If the spherical cap is assumed to be a segment of a sphere then the total plane angle it subtends at the bubble centre of curvature is 100° for the parameter range of interest. Under these circumstances the velocity of rise can then be related to the bubble volume ($U_0 = 0.79(gV^{\frac{1}{3}})^{\frac{1}{2}}$) and the equivalent diameter ($U_0 = 0.71(gD_e)^{\frac{1}{2}}$). By equating the buoyancy force ($\frac{1}{6}\pi D_e^3 g\Delta\rho$) to the drag force on the cap ($\frac{1}{2}\rho U_0^2 \frac{1}{4}\pi D_e^2 C_D$), where C_D is a drag coefficient, one finds:

$$C_D = \frac{4}{3Fr^2} \approx \tfrac{8}{3} \quad \text{where} \quad Fr = \frac{U_0}{(gD_e)^{\frac{1}{2}}}. \tag{2}$$

There are many practical situations where a bubble, such as the one discussed above, may, during some part or all of its trajectory, be forced to rise in a more

constricted geometry. A number of cases are discussed in Clift *et al.* (1978, chapter 9); these include bubble rise in tubes of various diameter (D), such that an extensive range of D_e/D is covered, as well as a range of tube inclinations. However, the one case that appears to be missing is the one that is the subject of this paper, namely, bubble rise under an inclined plate placed in a large container. Here the effects of all of the walls, except the inclined one, are negligible. As we will see, this case has some features in common with the well-established spherical-cap regime and some quite subtle differences. It is related to the study of Maneri & Zuber (1974) who, however, constrained the bubbles laterally by allowing them to rise between vertical sidewalls that were quite close together (see §2).

In §2 we present the experimental apparatus and procedure, in §3 the basic results, in §4 a simple theory and in §5 we discuss the dynamics of the flow and its relationships to existing results.

2. Apparatus and procedure

The water-filled tank used in these experiments is shown in figure 1. It consists of a Lucite box 1.22 m long, of cross-section 32 cm (in the experiments Maneri & Zuber (1974) this dimension was of the order of 1 cm) × 17 cm, hinged part way along one long side so that it could be held at various angles to the horizontal (α) from 5° to 90°. Bubbles of known volume were injected by hypodermic syringe and needle into an inverted hemispherical cup which was then rapidly turned to release a bubble into the lower part of the tank. The motion of the bubble was followed by recording its image on video tape using a camera, with an internal clock, mounted perpendicular to the inclined surface. Under some circumstances images were recorded by a 35 mm SLR camera with a motor-drive and flash attachment. The bubble motion was timed through 54 cm of its motion after it had first travelled approximately 60 cm from the point of injection and had reached its asymptotic, constant velocity. The room temperature was maintained at 22 ± 1 °C. Tests were run at angles (α) of 5, 10, 15, 20, 25, 30, 35, 45, 50, 60, 70, 80, 85 and 90° and bubble volumes (V) from 5 to 60 ml at intervals of 5 ml.

3. Results

The results take several forms. First, observations of the bubble shape as seen by the perpendicular camera and from these measurements of two characteristic lengths, the width, W, and the radius of curvature of the leading edge, R (figure 2). Secondly, observations of the bubble shape as seen by a camera photographing the sideview of the bubbles. From these pictures measurements of the ellipticity of the bubble as well as the radius of curvature of the 'nose'. Thirdly, measurements of the rise velocity, presented in appropriate non-dimensional form.

Figure 2 shows sketches of three moderately large bubbles at small, moderate and large angles of inclination in order to present clearly the shape taken by these bubble types. A series of top-view photographs is shown in figure 3, forming a matrix for angles of 5, 20, 50, 70 and 90° and volumes of 5, 10, 25 and 55 ml. The shapes sketched in figure 2 are seen to be typical of the shapes for the larger volumes with a gradual transition to an almost cylindrical bubble, with its long axis (W, figure 2) perpendicular to the direction of motion, at the smallest volume where surface tension and contact angle effects must become important. In these latter cases the Weber number ($U_0^2 D_e \rho/\sigma$) is of order 10 compared to $O(100)$ for the larger bubbles

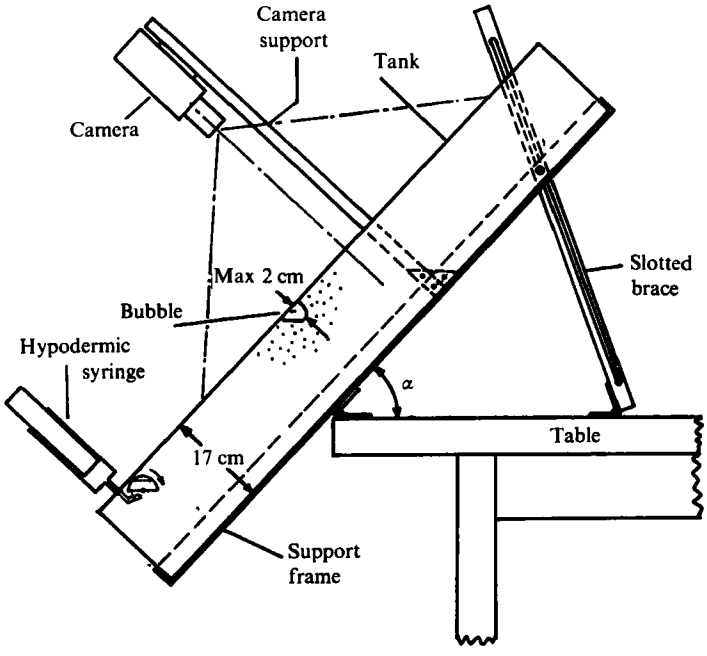

FIGURE 1. Side view of the apparatus.

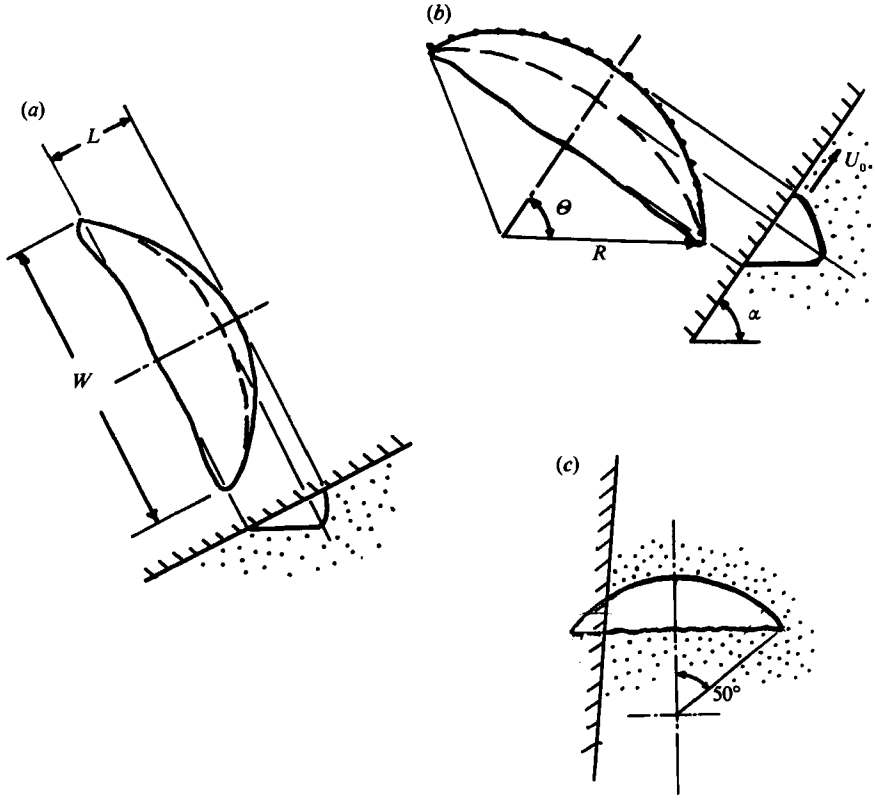

FIGURE 2. The geometry of the bubbles at low, moderate and high angles of tank inclination. Showing the definition of various quantities discussed in the text.

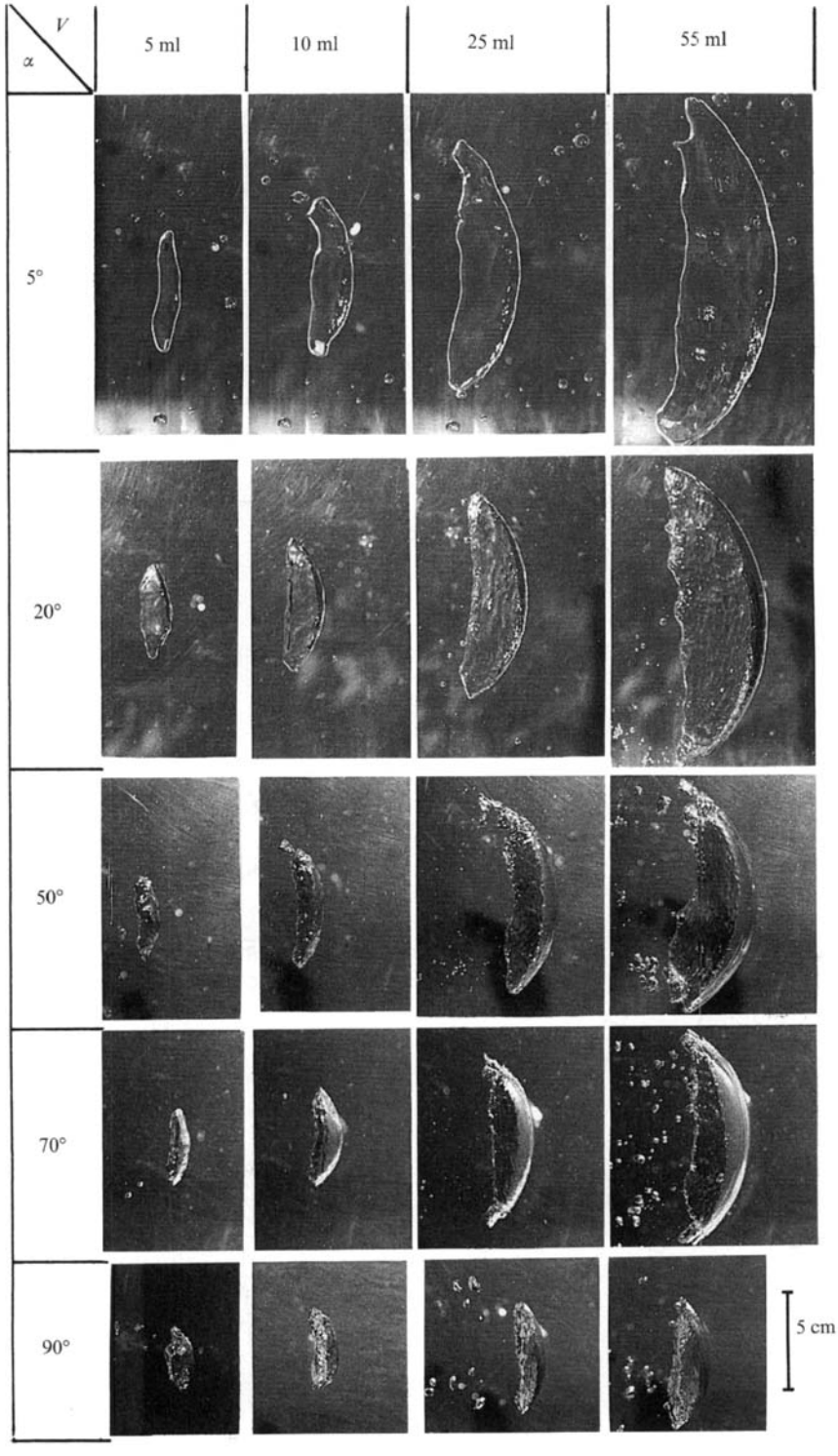

FIGURE 3. Plan view photographs of the bubbles at various values of α and bubble volume (V).

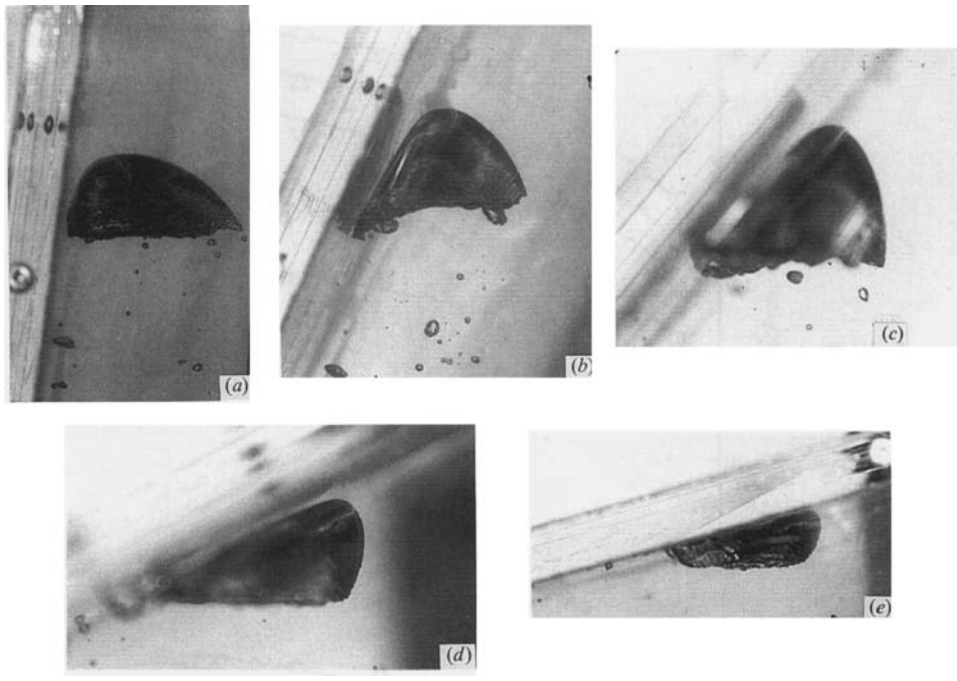

FIGURE 4. Side view photographs for $V = 60$ ml and values of α (*a*) 82°, (*b*) 65°, (*c*) 50°, (*d*) 25°, and (*e*) 15°.

and hence one might expect the shape to be affected. Curiously, as we will see, the non-dimensional velocity of rise is only slightly modified by this difference in shape and the low value of the Bond number.

Photographs of the side view of a few representative bubbles are shown in figure 4. Gravitational flattening of the bubble is apparent for the smaller inclination angles and larger volumes, the shape is very reminiscent of a form of boomerang for those who like visual images of such, moderately complex shapes. At angles close to 90° the shapes approach those of 'classical' spherical cap bubbles with centres displaced somewhat from the wall (figures 2*c* and 4*a*). Detailed measurements of these shapes will be presented later when the need for them enters more naturally, for the moment the qualitative results given above are sufficient as an introduction to this section.

Velocity-of-rise measurements form the core of this presentation. A selection of the raw data is shown in figure 5(*a*,*b*) where we show data for nine of the fourteen inclination angles used. These data must now be made dimensionless in a suitable way, one of which we show in figure 6. Here we plot $Fr_1 = U_0/(gV^{\frac{1}{3}}\sin\alpha)^{\frac{1}{2}}$ as being the most logical from both dynamical and dimensional points of view and which is based on the independent variables. Rather surprisingly, except for the smallest angle, the Froude number is sensibly constant over the whole range of bubble volumes, although the scatter in at least one case is somewhat large. As pointed out before this result holds for bubble shapes that appear to be rather different as the bubble volume is reduced. Only at the smallest angle (5°) can any consistent trend be seen and then it only amounts to a $\pm 5\%$ change from the mean value. With these observations in mind we can then plot Fr_1 *vs.* α for all the data, where the error bars represent both the trend of the Fr_1 *vs.* V curves and the data scatter. Figure 7 is the resultant plot where we show also the Froude number (Fr_2), uncorrected for inclination, and the

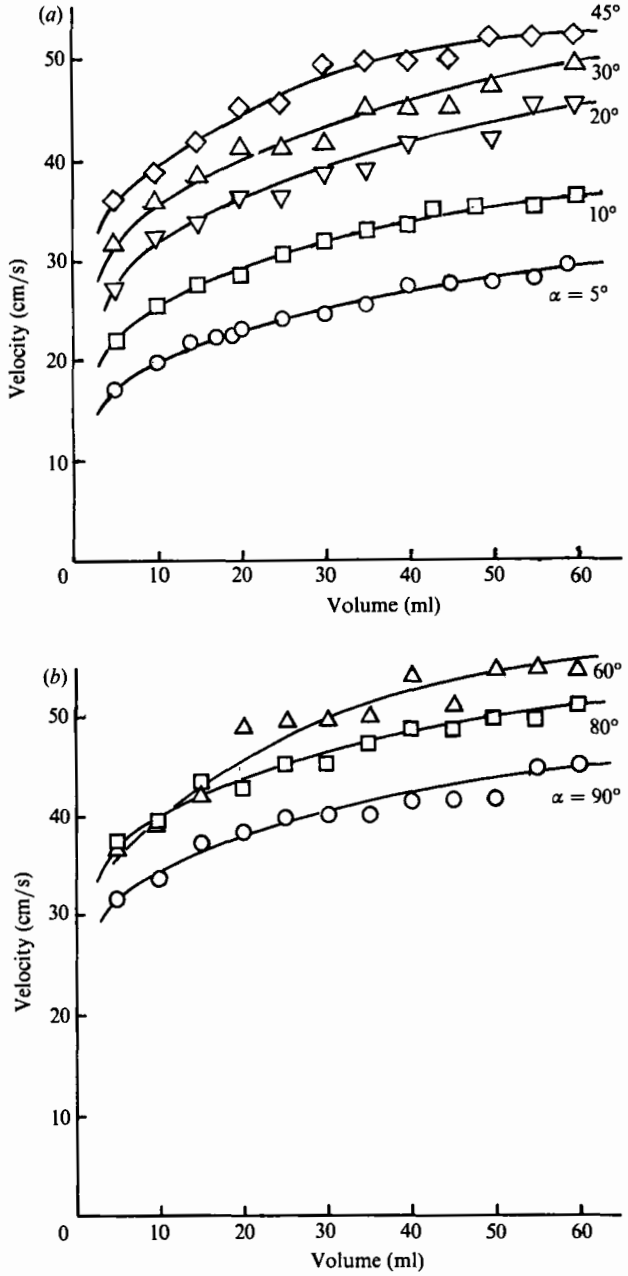

FIGURE 5. Bubble velocity (U_0) as a function of bubble volume for various values of α.

drag coefficient C_d calculated from a modified equation (2), i.e. $C_d = 1.65/Fr_1^2$ where, in this case, both the drag and the buoyancy act parallel to the plate and we have used the relationship between V and D_e given in §1. As $\alpha \to 0$ Fr_2 must also tend to zero, while Fr_1 tends to a finite value of 1.6, and C_D to 0.64.

Alternative ways of plotting these data are available if one uses dependent variables. As a first step we present measurements of the bubble width (W) versus $V^{\frac{1}{3}}$, figure 8. For the range of bubble volumes used here the relationship between the two

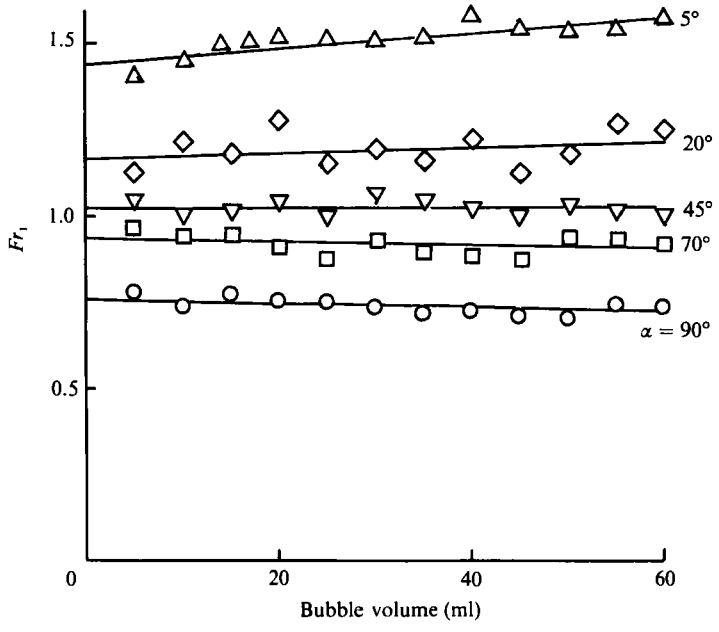

FIGURE 6. Froude number (Fr_1) versus bubble volume for several values of α.

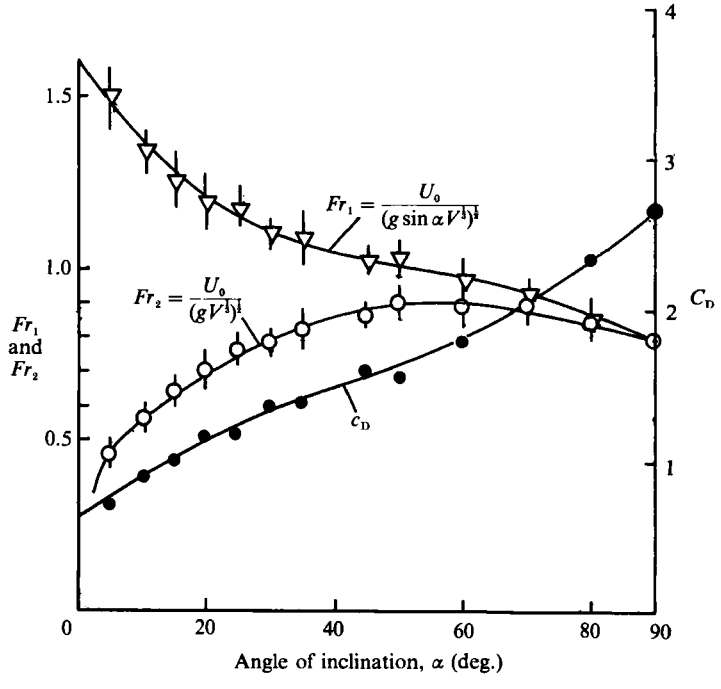

FIGURE 7. Fr_1, Fr_2 and drag coefficient (C_D) versus angle of inclination.

is a straight line which, however, does not pass through the origin, i.e. for smaller values of $V^{\frac{1}{3}}$ the relationship is closer to a quadratic function. Replotting the velocity data using W as a lengthscale gives the results shown in figure 9. Where we note especially that over a wide range of inclination angles the Froude number

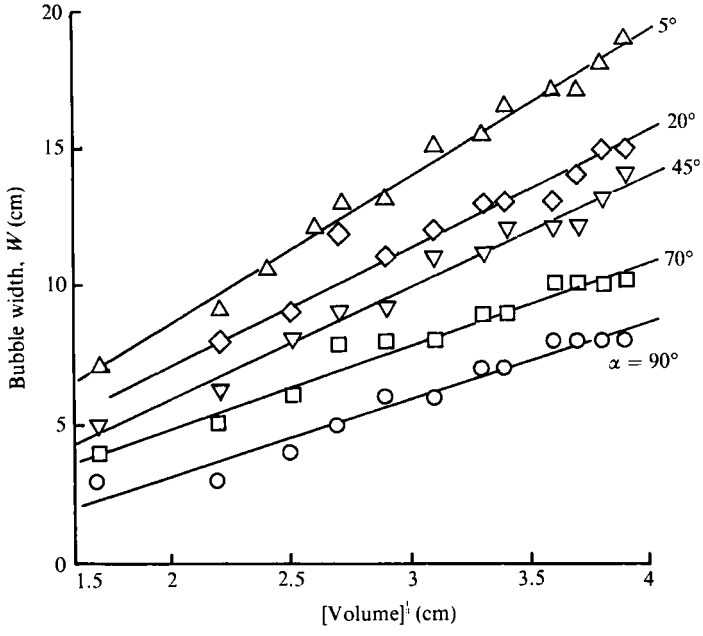

FIGURE 8. Bubble width (W), in the plan view, versus $V^{\frac{1}{3}}$ for several values of α.

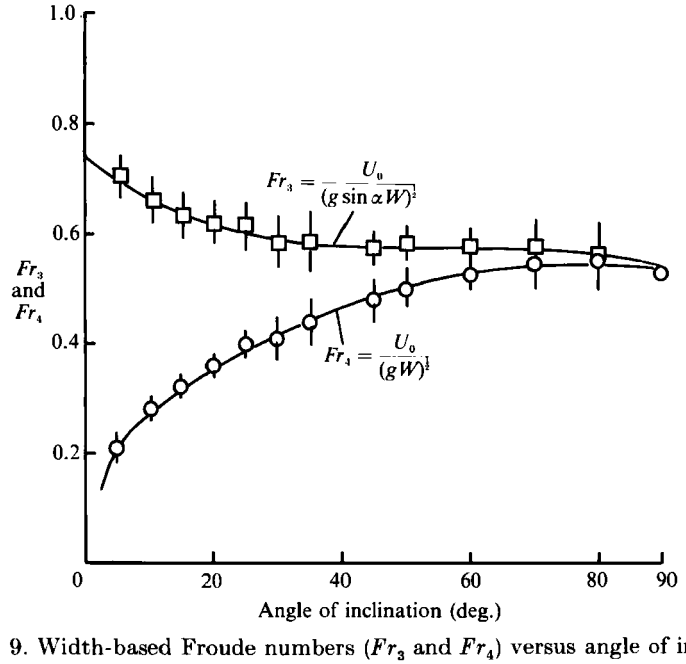

FIGURE 9. Width-based Froude numbers (Fr_3 and Fr_4) versus angle of inclination.

$(Fr_3) = U_0/(gW \sin \alpha)^{\frac{1}{2}}$ is sensibly constant at a value of 0.59 and tends to 0.74 as α tends to zero.

From a fundamental point of view, and to make comparison with the classical Davies & Taylor (1950) result mentioned in §1, the most interesting aspect of these flows is the appearance, in this case too, of a leading edge of essentially constant

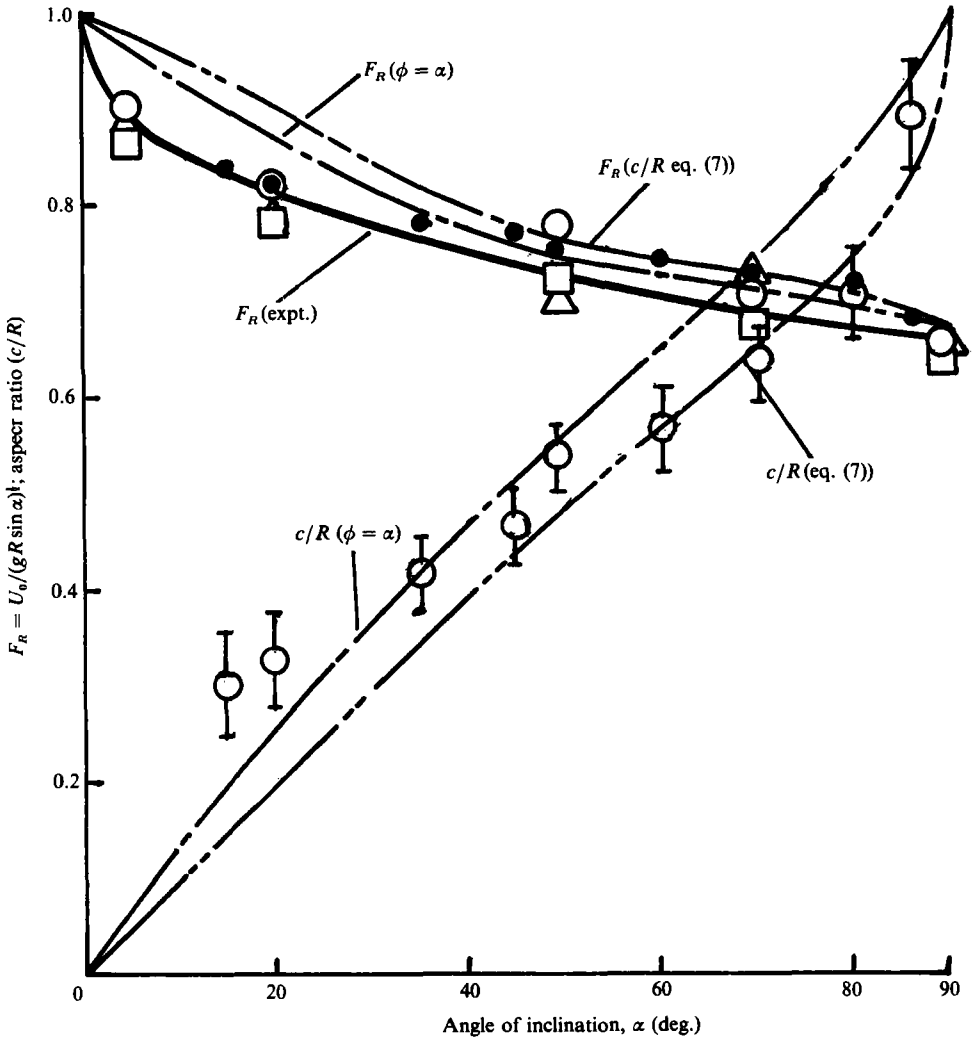

FIGURE 10. ○, □, △, Froude number F_R based on the radius of curvature of the leading edge of the bubble (R) versus angle of inclination for several values of bubble volume greater than 10 ml. ⚲, Measured values of the ellipticity of the bubble transverse cross-section (c/R). Calculated values of c/R; – – –, using the matching condition at $\phi = \alpha$; —·—·—, using an integral condition (equation 7). Values of F_R using the values of c/R calculated from the first two conditions above (—·—) and (—···—). ●, Values of F_R calculated from the measured values of c/R (⚲).

radius of curvature (R). Constructing a Froude number based on this lengthscale (the open symbols on figure 10) shows that it varied from the well-established value of about 0.65 for $\alpha = 90°$ to 1.0 as $\alpha \to 0$. We present a theory that appears to explain this result in §4.

Finally, we can quantify the changes in the shape of the leading edge of the bubble in two ways. Firstly by plotting, on figure 11, the ratio W/R and at the same time calculating the half-angle (Θ) subtended by the segment of the circle that makes up this leading edge, where these quantities are defined on figure 2. Here again we obtain the well-established value for $\alpha = 90°$, with some scatter, and a maximum angle of 66°, i.e. the deepest segment, for an inclination around 50°, where the velocity, for a given volume, is also a maximum (figure 7). Secondly, by assuming that the vertical

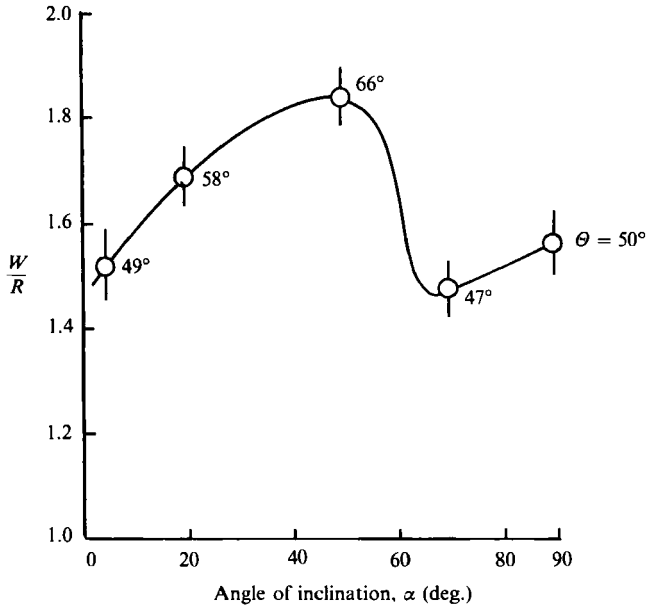

FIGURE 11. Bubble geometrical parameter (W/R) and the corresponding values of Θ (figure 2) versus angle of inclination, averaged over bubble volumes greater than 10 ml.

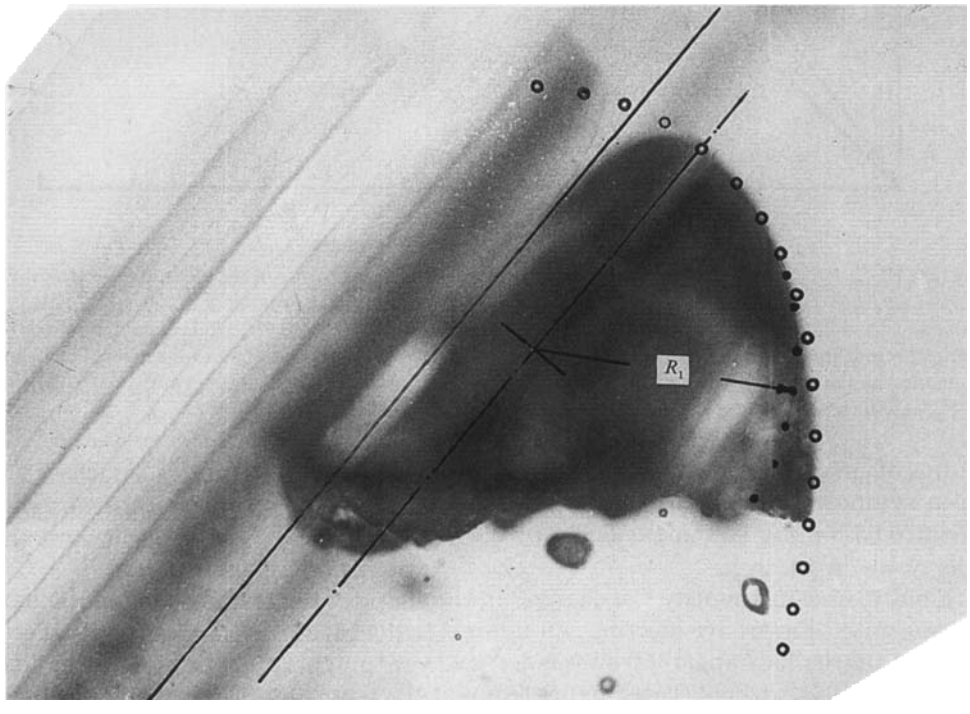

FIGURE 12. Experimental matching of an ellipse with $c/R = 0.53$, on a photograph of the side view of a 60 ml bubble at $\alpha = 50°$. Showing, also, the radius of curvature of the bubble nose, R_1, for this value of c/R.

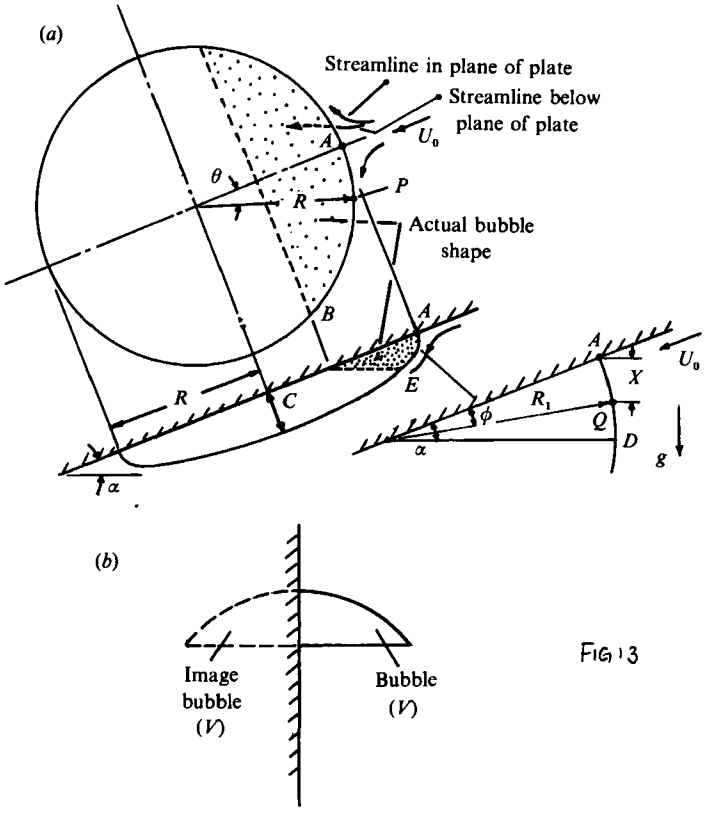

FIG. 13

FIGURE 13. (*a*) Bubble geometry related to that of an oblate spheroid moving edge-on to the flow. Definition of quantities used in §4. Anticipated bubble shape for values of $\alpha \approx 90°$. Here the effective bubble volume would have been $2V$ and the bubble rise velocity a factor of $2^{\frac{1}{6}}$ greater than the velocity of rise of an isolated bubble of volume V. As shown in figures 2(*c*) and 4(*a*) this configuration is not seen in these experiments.

cross-section of the bubble is an ellipse, we can measure its ellipticity as a function of α. A typical fitting of this type is shown in figure 12 where, for $\alpha = 50°$, we fit an ellipse with $c/R = 0.53$ to the observed shape, we show also the equivalent radius curvature of the nose region, a quantity needed for the theoretical development which follows. The values of c/R at various angles of inclination (α) are shown on figure 10 (the symbols $\dot{\varphi}$). These results then constitute the basic findings of this study, comments on their significance follow in §§4 and 5.

4. Theory

Using the results shown in figure 10 as a basis we present a theoretical explanation that appears to represent many elements of the observations in a moderately accurate fashion. It is based on the method used by Davies & Taylor (1950) and at the same time points out one limitation of their approach. As shown in figure 13(*a*) we assume that the flow over the leading surface of the bubble is that over an oblate spheroid moving parallel to its circular cross-section, with the ellipticity of the transverse cross-section depending on the angle at which the bubble rises.

The flow field and hence the pressure distribution can be found, using ellipsoidal

coordinates, in Lamb (1945, §132). This formulation however is rather cumbersome and so we use results due to Munk contained in Durand (1932) in which he states the simple rule that 'the velocity on the surface of any ellipsoid moving parallel to one of its principal axes, is given by projecting the maximum velocity onto the tangent plane at the point of interest.' The maximum velocity, of course, occurs at the elliptic equator of the ellipsoid and is constant around it. As a result, by allowing the maximum fluid velocity to be represented by kU_0, we can calculate the pressure distribution along the circular cross-section of our oblate spheroid, i.e. along the curve APB of figure 13(a). In order for the pressure along this line to be constant, since the pressure within the bubble is also constant, the calculated decrease in static pressure due to the flow has to be balanced by the increase in hydrostatic pressure. We obtain the result that there is one and only one velocity of rise for each value of θ which can satisfy this condition. The resulting equations can be written, assuming that the reference level is at the point A, as:

$$\tfrac{1}{2}k^2U_0^2\sin^2\theta = gR(1-\cos\theta)\sin\alpha. \tag{3}$$

Simplifying gives:

$$\frac{U_0^2}{gR\sin\alpha} = \frac{2}{k^2(1+\cos\theta)}.$$

Following Davies & Taylor (1950) we choose, arbitrarily, to satisfy this equation exactly only at $\theta = 0$ so that:

$$\frac{U_0}{(gR\sin\alpha)^{\frac{1}{2}}} = \frac{1}{k}. \tag{4}$$

Note that for a sphere $k = \frac{3}{2}$, and we recover the Davies–Taylor result in this limit. Clearly k varies from this value of $\frac{3}{2}$ when $\alpha = \frac{1}{2}\pi$ to a value of 1 when $\alpha = 0$, i.e. when the bubble is completely flattened by the effect of gravity, and we ignore contact angle and surface tension effects. In order to calculate values between these limits we need to know the ellipticity of the cross-section at each value of α. However, before performing this calculation we note that, in general, once the ellipticity is known, k can be found as follows:

Munk in Durand (1932) gives the value of the maximum velocity as

$$U_m = \left(1+\frac{\alpha_0}{2-\alpha_0}\right)U_0 \equiv (1+k_0)\,U_0 \equiv kU_0,$$

where, in general

$$\alpha_0 = abc\int_0^\infty \frac{\mathrm{d}\lambda}{(a^2+\lambda)^{\frac{3}{2}}(b^2+\lambda)^{\frac{1}{2}}(c^2+\lambda)^{\frac{1}{2}}}$$

when the ellipsoid is moving in the direction of the a-axis, and a, b, and c are its semi-axes.

It turns out that k_0 is simply the coefficient of apparent mass of the ellipsoid, e.g. for a sphere $\alpha_0 = \frac{2}{3}$ and $k_0 = \frac{1}{2}$.

Furthermore the relationship between α_0, and hence k_0 and k, and the body shape can be found in several references, the simplest being presented in Lamb (1945, §373, equation 14) for the oblate spheroid of interest here, as:

$$\alpha_0 = \frac{(1-e^2)^{\frac{1}{2}}\sin^{-1}e}{e^3} - \left(\frac{1-e^2}{e^2}\right)^2,$$

where e is the eccentricity of the cross-section, $e = (R^2-c^2)^{\frac{1}{2}}/R$ in our notation (figure 13a).

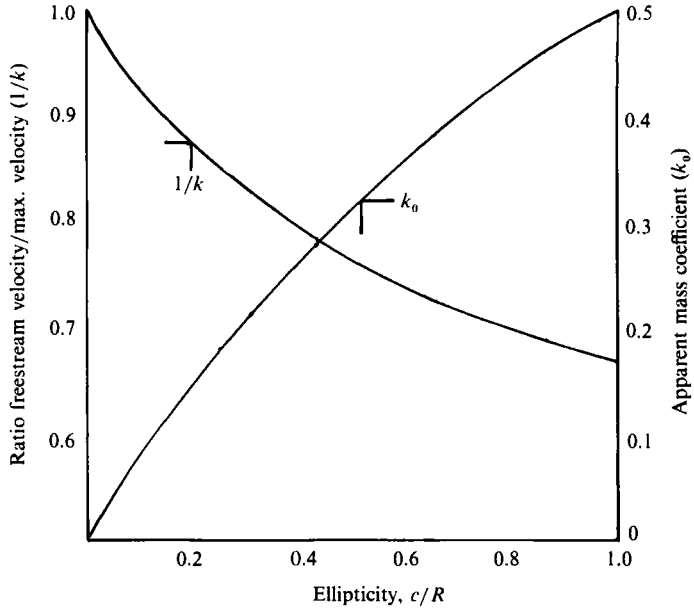

FIGURE 14. Apparent mass coefficient (k_0) and velocity ratio ($1/k = U_0/U_m$) versus cross-section ellipticity c/R.

Values of k_0 and $(k_0+1)^{-1} \equiv k^{-1}$ are a function of c/R as shown in figure 14.

With this background we are now in a position to calculate the shape of the cross-section. Assuming that the curve $AQDE$ can be represented locally by an arc of a circle (figure 13*a*) we can repeat the calculation that led to equation (4) in that case along the curve APB. Note that here the distance X of figure 13(*a*) is given by:

$$X = R_1 \sin\alpha - R_1 \sin(\alpha - \phi).$$

Expand the last term, simplifying and equating the hydrostatic pressure to the static pressure due to the flow we find:

$$\tfrac{1}{2}k^2 U_0^2 \sin^2\phi = gR_1 \sin\alpha(1-\cos\phi) + \cos\alpha \sin\phi], \tag{5}$$

but from equation (4) $k^2 U_0^2 = Rg\sin\alpha$ so that:

$$R_1((1-\cos\phi) + \cot\alpha \sin\phi) = \tfrac{1}{2}R\sin^2\phi,$$

or

$$R_1\left(\frac{1}{1+\cos\phi} + \frac{\cot\alpha}{\sin\phi}\right) = \tfrac{1}{2}R. \tag{6}$$

From this equation we can in principle, calculate R_1/R at the nose of the elliptic cross-section, which is related to c/R as $(R_1/R) = (c^2/R^2)$. Unfortunately, the Davies–Taylor procedure, of taking the limit $\phi \to 0$, cannot be applied here since the result is singular. In fact we note that the case considered by Davies–Taylor, i.e. $\alpha = \frac{1}{2}\pi$, is the only one which can be calculated using the technique they proposed! We are forced to use a different condition to estimate the ratio R_1/R. Two obvious possibilities come to mind: (i) evaluate the condition at $\phi = \alpha$; (ii) evaluate the condition in such a way that the surface pressure is zero in an average or integral sense over the whole surface, i.e. from (5) calculate

$$R_1 \int_0^\alpha (1 - \cos\phi + \cos\alpha \sin\phi)\, d\phi = \tfrac{1}{2}R \int_0^\alpha \sin^2\phi \, d\phi,$$

the result is:

$$\frac{R_1}{R} = \frac{c^2}{R^2} = \frac{1}{4}\frac{[\alpha - \frac{1}{2}(\sin 2\alpha)]}{[(\alpha - \sin\alpha) + \cot\alpha(1-\cos\alpha)]}. \tag{7}$$

The results of this calculation and those resulting from assumption (i) are shown in figure 10 together with the calculated values of $F_R = U_0/(gR\sin\alpha)^{\frac{1}{2}}$ using figure 14. Also shown on this figure are the values of F_R calculated using the procedure leading to figure 14 but using the measured values of c/R.

Note, also, that (5) can be used to describe the velocity of rise of the elliptical bubbles in the experiments of Maneri & Zuber (1974). As in the Davies–Taylor calculations two pieces of experimental evidence are needed: the radius of curvature of the nose and the ellipticity of the bubble, both of which could be extracted from their raw data.

5. Discussion and conclusions

Based on the large number of tests presented here it appears that a description of the flow based on inviscid dynamics is justified, in particular both the Reynolds number and Bond number are in the range where for spherical-cap bubbles this is true, except for the smallest volumes. As a consequence, as shown on figure 10, the data can be reduced using the radius of curvature of the leading edge as a lengthscale. For the spherical-cap case, and our case with $\alpha = 90°$, this means that the velocity of rise can be found by considering the inviscid, irrotational flow over a spherical surface, as already mentioned. Here on applying Bernoulli's equation, including the hydrostatic pressure, around the spherical surface and requiring that the resultant pressure be constant gives, to the first approximation, the Davies & Taylor (1950) result, while a second-order approximation was found by Collins (1966). It is of some interest that the velocity of rise is not $2^{\frac{1}{2}}$ times the velocity for a freely rising bubble based on the expectation that the vertical wall would become a plane of symmetry for a complete bubble of twice the experimental volume (figure 13*b*). The actual flow as shown in figure 2(*c*) is that around an almost complete spherical cap, of volume V displaced slightly from the wall.

In our case for angles of inclination away from 90° the bubble becomes distorted into what is, to a first approximation and near the stagnation point, half of an oblate spheroid (figure 13*a*), which remains self similar as the volume is varied at constant α. Under these circumstances a modified version of the Davies–Taylor calculation can be used to rationalize the experimental data. This approach is successful only at moderately large angle of inclination, at the smaller angles the ellipticity of the vertical cross-section is underestimated while the Froude number is overestimated. This is presumably due to the fact that surface tension and contact angle effects must become more important for the low velocities and severely truncated elliptical cross-sections involved.

The help of T. Al-Alshaikh in running many of the experiments reported here and in performing the initial data reduction is greatly appreciated. This work was supported in part by ONR Contract no. N00014-89-J-1400. The preliminary manuscript was written while the author held a Senior Scientist Fellowship of the Norwegian Science Foundation at the NHL, Trondheim. The generosity and help of Dr T. McClimans of the latter institution is acknowledged with gratitude. We are especially grateful to Professor M. van Dyke of Stanford University for pointing out the basic results of Munk contained in Durand (1932).

REFERENCES

CLIFT, R., GRACE, J. R. & WEBER, H. E. 1978 *Bubbles, Drops and Particles.* Academic.

COLLINS, R. 1966 A second approximation for the velocity of a large gas bubble rising in an infinite fluid. *J. Fluid Mech* **25**, 469–480.

DAVIES, R. M. & TAYLOR, G. I. 1950 The mechanics of large bubbles rising through extended fluids and through liquids in a tube. *Proc. R. Soc. Lond.* A **200**, 375–390.

DURAND, W. F. (ed.) 1932 *Aerodynamic Theory*, vol. 1, pp. 224–304. Dover.

LAMB, H. 1945 *Hydrodynamics.* Dover.

MANERI, C. C. & ZUBER, N. 1974 An experimental study of plane bubbles rising at inclination. *Intl J. Multiphase Flow* **1**, 623–645.

ZUKOSKI, E. E. 1966 The influence of viscosity, surface tension and inclination angle on the motion of long bubbles in closed tubes. *J. Fluid Mech.* **25**, 821–837.